Supplementary Information (SI) for Journal of Materials Chemistry A.

Supplementary Information

Unlocking exceptional sodium ion storage capability of manganese dioxide via controllable incorporation of cation vacancies

Peng Gao[1,2,3 #,*], Jiaofeng Yang[4 #], Kang Luo[1], Jinlong Ke[1]

[1]College of Materials Science and Engineering, Hunan Joint International Laboratory of Advanced Materials and Technology for Clean Energy, Hunan University, Changsha 410082, China

[2]Research Institute of HNU in Chongqing, Chongqing 401120, China

[3]Greater Bay Area Institute for Innovation, Hunan University, Guangzhou 511300, China

[4]Hunan Communications Research Institute Co. Ltd., Changsha 410015, China

Table S1 Summary of types and concentrations of doped ions. The molar ratios of X:Mn are denoted as the ratios of cations in precursor solutions over Mn in $MnSO_4$ respectively.

Samples	Doped ions (X)	Molar ratios (X:Mn)
α-MnO_2	Co	0.2:1, 0.5:1, 1:1, 2:1, 3:1
	Mg	0.5:1, 1:1, 2:1, 3:1
	Zn	0.5:1, 1:1, 2:1, 3:1
δ-MnO_2	Co	0.1:1, 0.25:1, 0.5:1, 1:1
	Mg	0.5:1, 1:1, 2:1, 3:1
	Zn	0.5:1, 1:1, 2:1, 3:1

Table S2 Summary of the parameters for acid/alkaline-treatment of Co/Mg/Zn doped α-MnO_2

Samples	Acid/alkaline solution type	Acid/alkaline solution concentration (M)	Treatment time (h)
Co-doped α-MnO_2（0.5:1）	HCl	1	8
Co-doped α-MnO_2（0.5:1）	HCl	1	24
Mg-doped α-MnO_2（1:1）	HCl	1	8
Mg-doped α-MnO_2（1:1）	HCl	1	24
Zn-doped α-MnO_2（2:1）	NaOH	1	8
Zn-doped α-MnO_2（2:1）	NaOH	1	24

Table S3 Summary of the parameters for acid/alkaline-treatment of Co/Mg/Zn doped δ-MnO_2

Samples	Acid/alkaline solution type	Acid/alkaline solution concentration (M)	Treatment time (h)
Mg-doped δ-MnO_2（1:1）	HCl	1	8
Mg-doped δ-MnO_2（1:1）	HCl	1	24
Zn-doped δ-MnO_2（1:1）	NaOH	1	1
Zn-doped δ-MnO_2（1:1）	NaOH	1	4
Zn-doped δ-MnO_2（1:1）	NaOH	1	8
Zn-doped δ-MnO_2（1:1）	NaOH	1	24

Supplementary Note S1: structure characterizations and electrochemical performance evaluation of pure α- and δ-MnO_2.

The as-prepared pure α- and δ-MnO_2 exhibit typical rod- and sheet-like morphologies (Fig. S1), characteristic of their crystal structures. The X-ray diffraction (XRD) patterns demonstrate the formation of pure phase. As shown in Fig. S2, all diffraction peaks can be indexed to the structures of α-MnO_2 (ICDD Card No. 44–0141) and δ-MnO_2 (ICDD Card No. 80–1098). The typical Raman spectra of α-MnO_2 exhibits two strong peaks centered at ~580 cm^{-1} and ~632 cm^{-1}, which are corresponding to the Mn-O vibrations along the chain and perpendicular to the chain, in agreement with previous reports. Similarly, the two peaks located at ~562 cm^{-1} and ~627 cm^{-1} in δ-MnO_2 can be assigned to the Mn-O vibrations in the basal plane of [MnO_6] sheets and that in the MnO_6 octahedra (Fig. S3). Thus, the Raman spectra further indicate successful synthesis of pure phase α- and δ-MnO_2. Nitrogen adsorption–desorption measurements were also performed to characterize the pore structures and obtain the specific surface areas (SSA) of the as-synthesized samples (Fig. S4). Both samples exhibit well-defined type IV-like isotherms with a H2-hysteresis loops, indicating the presence of mesopores according to the IUPAC classification. The Brunauer–Emmet–Teller (BET) SSA were 50 and 149 m^2/g for α- and δ-MnO_2 respectively, which are consistent with their apparently different morphologies. The large SSA of δ-MnO_2 is mainly originated from its porous "house-of-cards" structure formed through nanosheet stacking, which will also benefit the infiltration of electrolyte ions and therefore enhancement of charge storage performance.

The Na^+ storage properties of as-prepared α- and δ-MnO_2 were further evaluated, with the results shown in Fig. S5 and S6. The cyclic voltammetry (CV) curves obtained at low scan rate (2 mV/s) for both samples exhibit largely rectangular shapes in the potential window from 0 to 1 V, which indicates capacitive behaviour and successive redox reactions. The presence of broad redox peaks indicate that Na^+ intercalation is an active and detectable charge storage mechanism for these specimen. With increasing scan rate, the CV curves are gradually deviated from rectangular shape, which is related to the impeded ion diffusion under high rate. Besides, the charge transfer resistances are similar for both samples, indicating negligible effects of the electrode's crystal structure and morphologies on charge storage process. However, their specific capacitances are significantly different. At 0.2 A/g current density, the specific capacitance of δ-MnO_2 is ~179 F/g, which is 4.7 times higher than that of α-MnO_2 (~38 F/g). Meanwhile, the δ-MnO_2 exhibits better rate performance. This is because the layered structure of δ-MnO_2 could provide fast ion diffusion channels, meanwhile the porous "house-of-cards" structure could provide more sites for ion absorption, both therefore synergistically improves the specific capacitance and rate capability of δ-MnO_2 electrode.

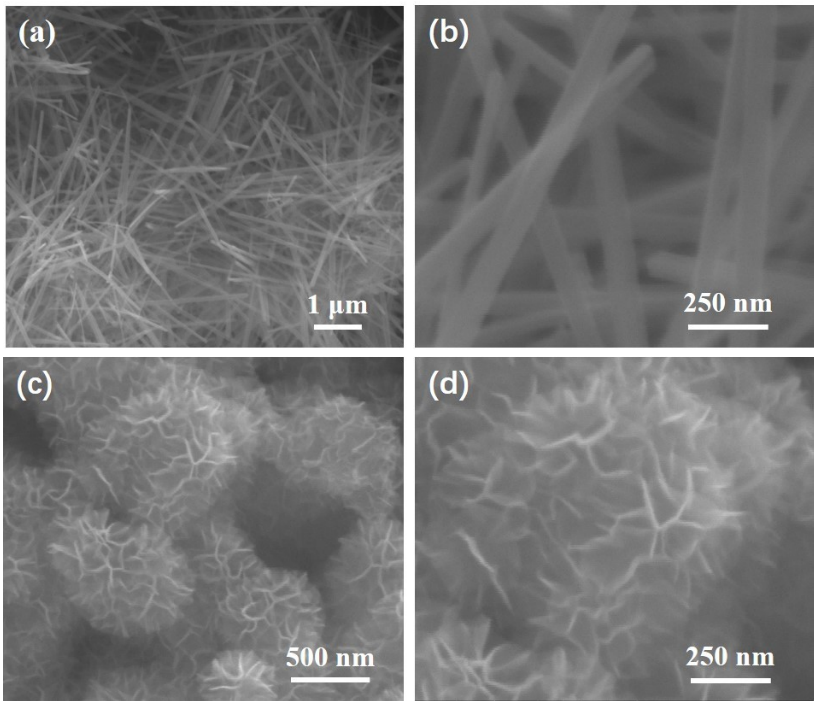

Fig. S1 Typical SEM morphologies of (a, b) pure α-MnO_2, and (c, d) pure δ-MnO_2.

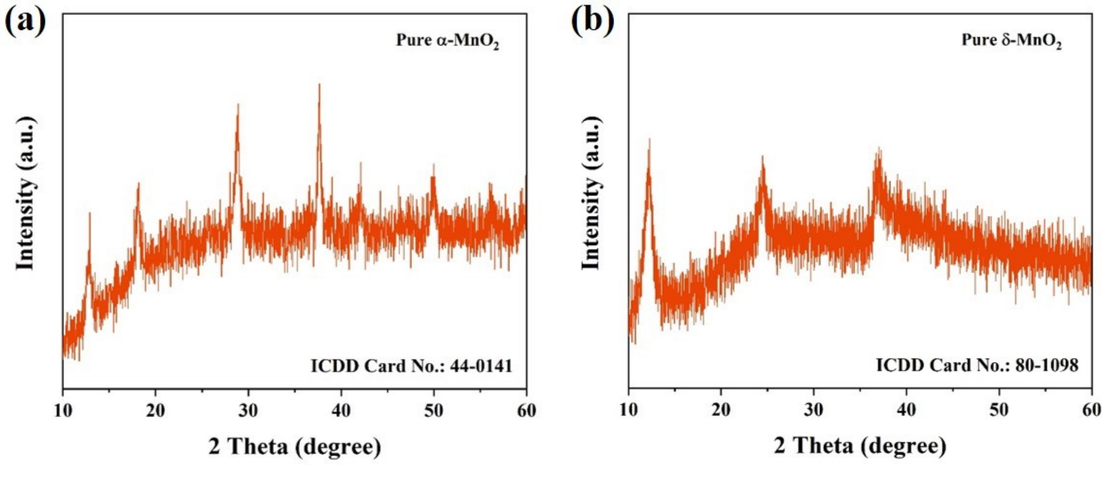

Fig. S2 X-ray diffraction (XRD) patterns of (a) pure α-MnO_2, and (b) pure δ-MnO_2.

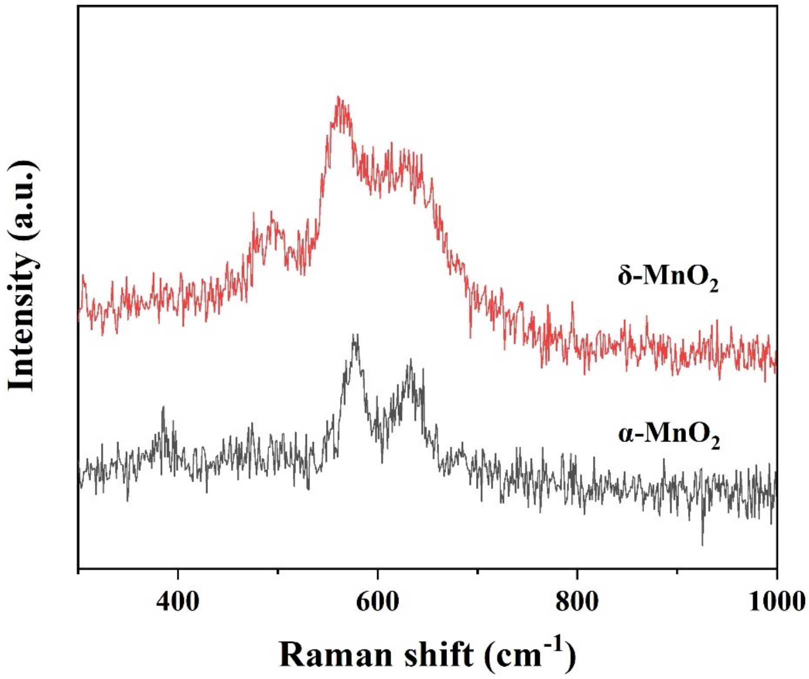

Fig. S3 Raman spectra of pure α-MnO_2 and δ-MnO_2.

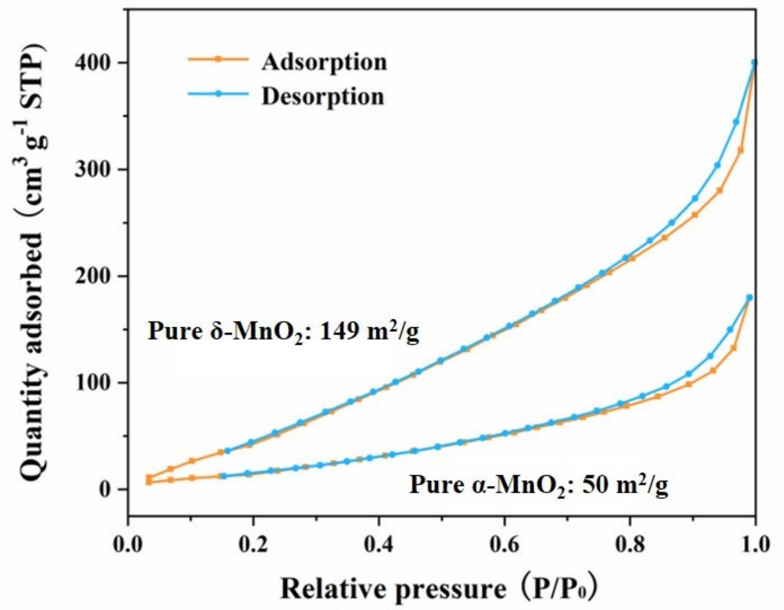

Fig. S4 N_2 adsorption–desorption isotherms of pure α-MnO_2 and δ-MnO_2.

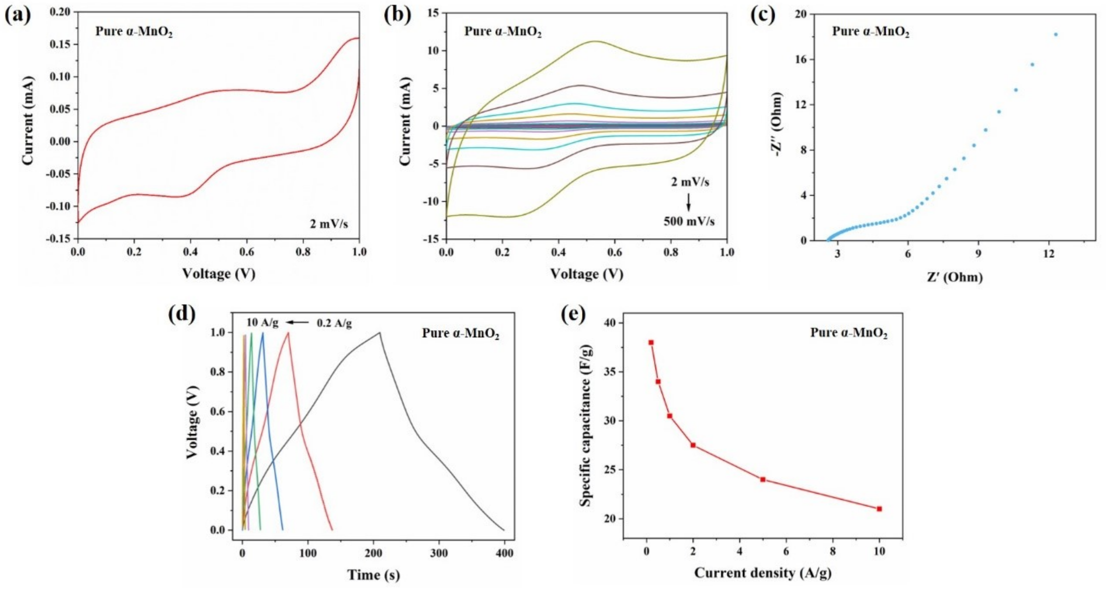

Fig. S5 (a, b) Cyclic voltammetry (CV) curves measured at 2-500 mV/s scan rates and in 0-1 V voltage range, (c) Nyquist plots, (d) Galvanostatic charge-discharge (GCD) curves obtained at 0.2-10 A/g current densities, and (e) Specific capacitances at various current densities of pure α-MnO_2.

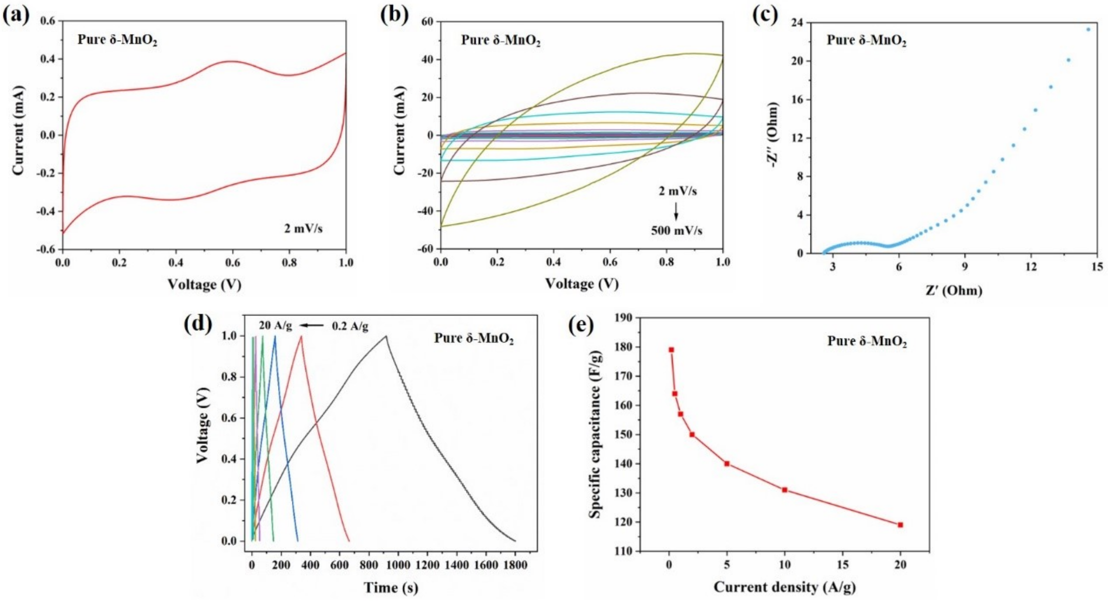

Fig. S6 (a, b) CV curves measured at 2-500 mV/s scan rates and in 0-1 V voltage range, (c) Nyquist plots, (d) GCD curves obtained at 0.2-20 A/g current densities, and (e) Specific capacitances at various current densities of pure δ-MnO_2.

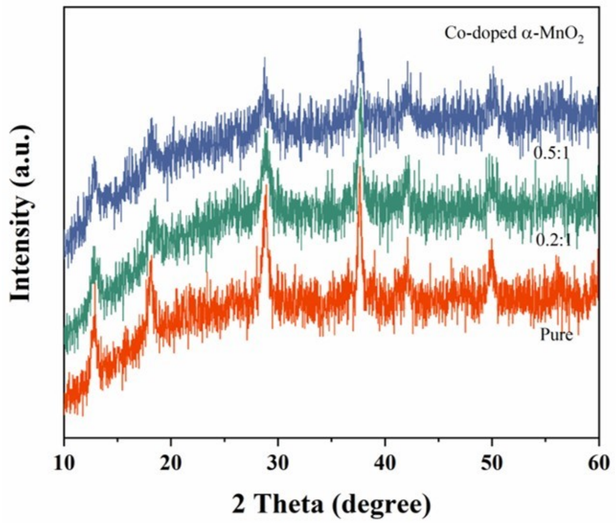

Fig. S7 XRD patterns of the pure and Co-doped α-MnO_2.

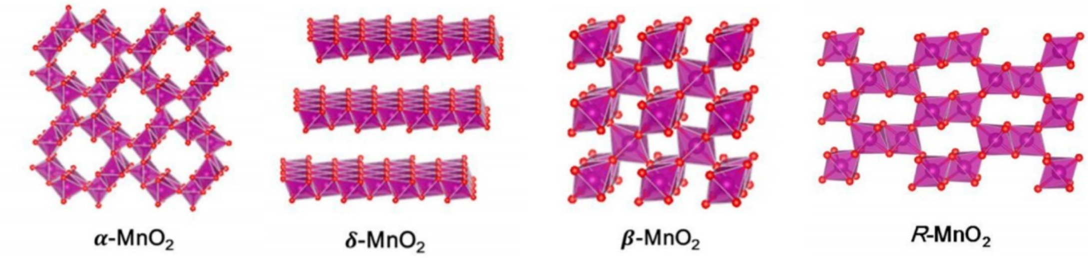

Fig. S8 Crystal structures of MnO_2 with different polymorphs.

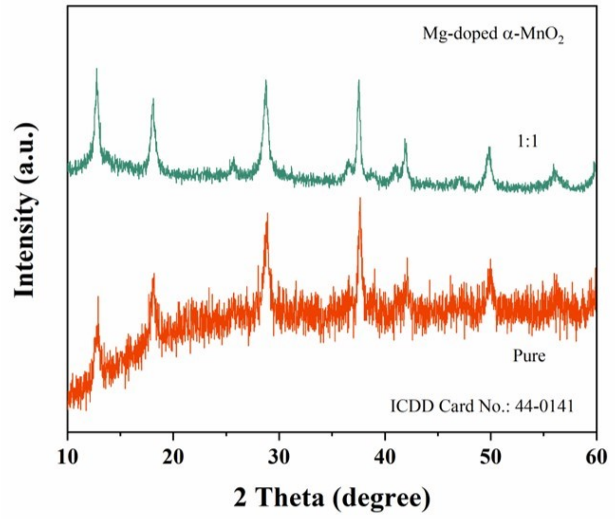

Fig. S9 XRD patterns of the pure and Mg-doped α-MnO_2.

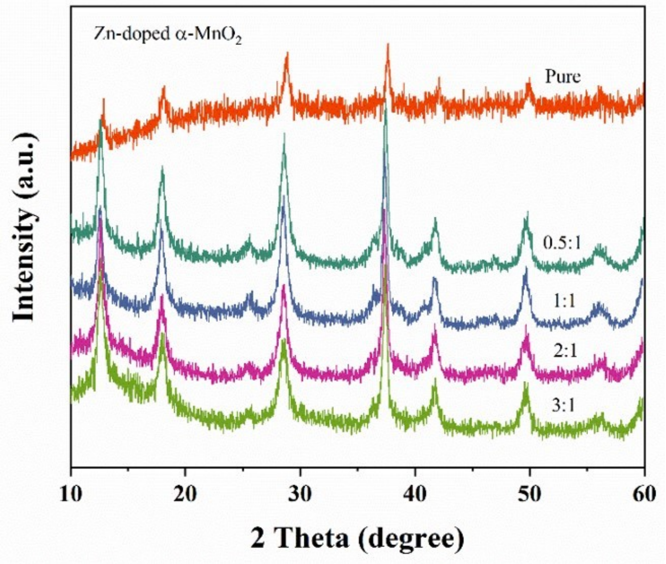

Fig. S10 XRD patterns of the pure and Zn-doped α-MnO_2.

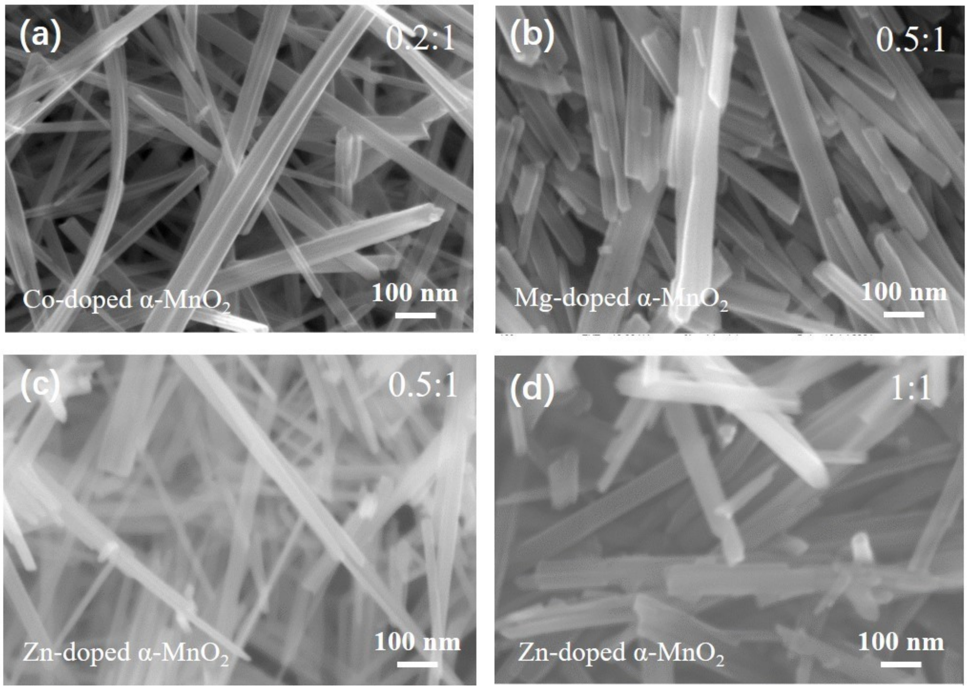

Fig. S11 SEM images of Co, Mg, and Zn-doped α-MnO_2.

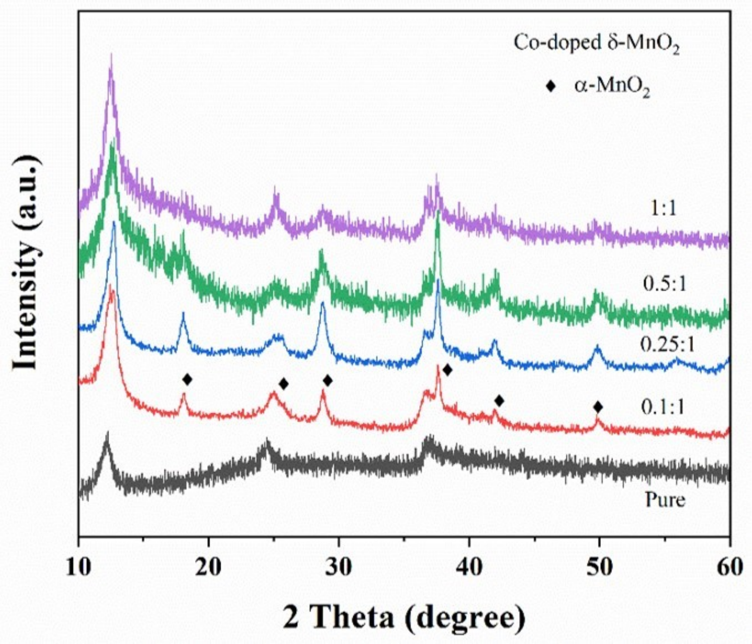

Fig. S12 XRD patterns of the pure and Co-doped δ-MnO$_2$.

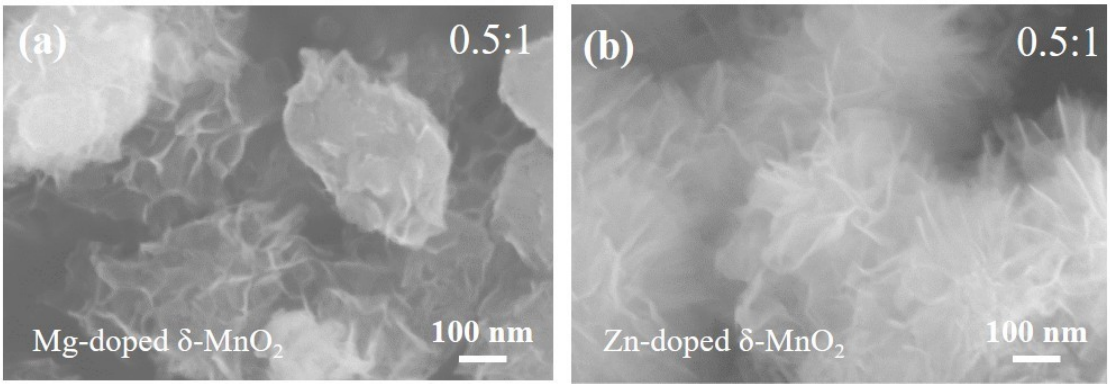

Fig. S13 SEM images of (a) Mg, and (b) Zn-doped δ-MnO$_2$.

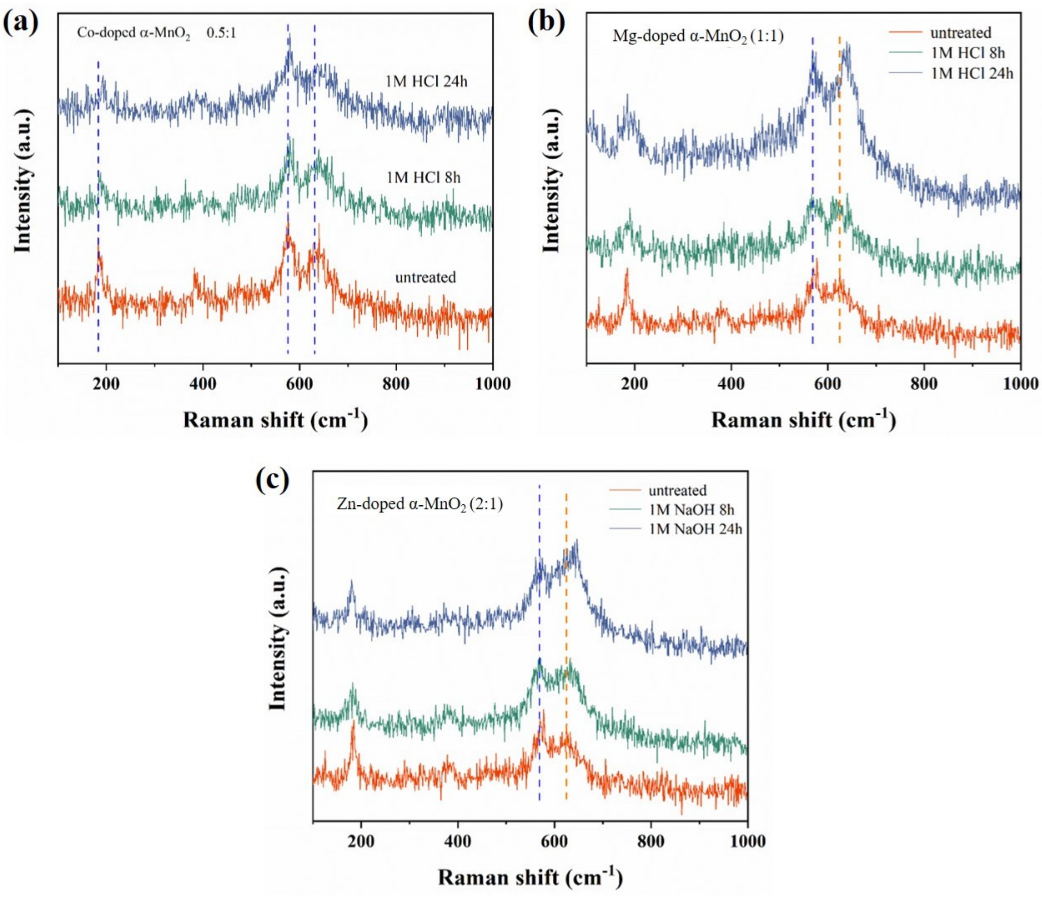

Fig. S14 Raman spectra of (a) Co-doped α-MnO_2 (0.5:1), (b) Mg-doped α-MnO_2 (1:1), and (c) Zn-doped α-MnO_2 (2:1) with different acid/alkaline treatment conditions.

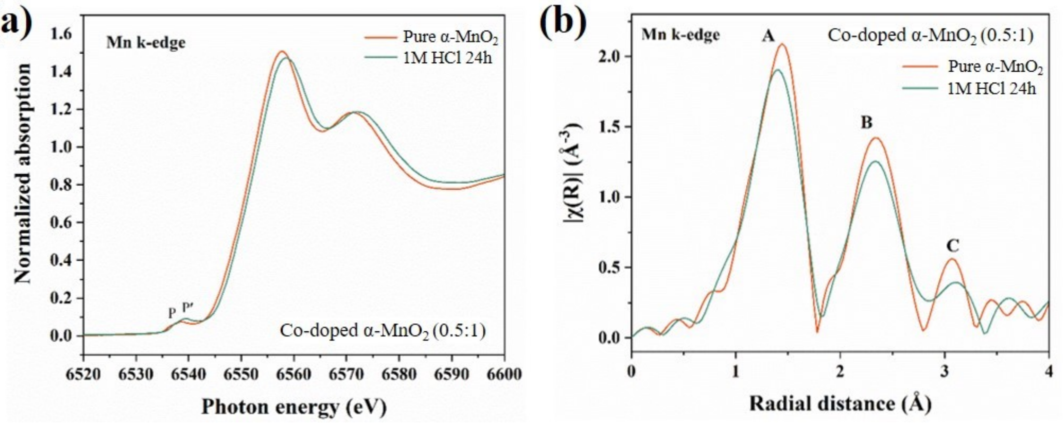

Fig. S15 (a) Normalized Mn K-edge XANES spectra, and (b) Mn K-edge EXAFS spectra of Co-doped α-MnO_2 (0.5:1) with different acid treatment conditions.

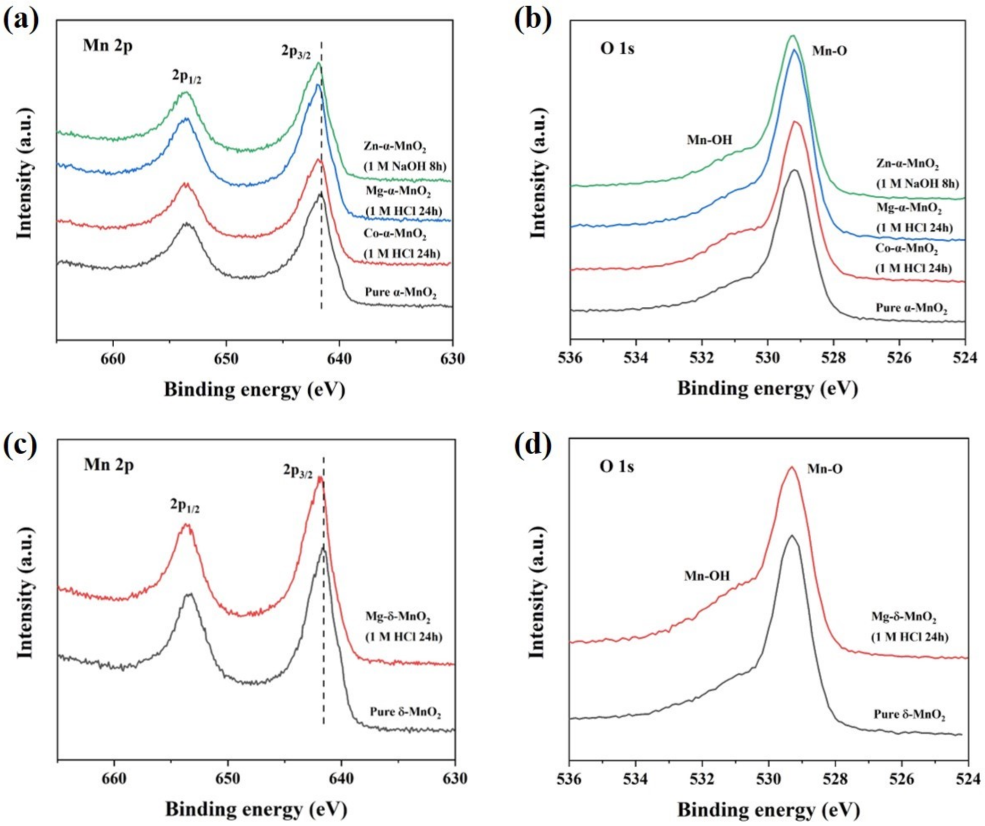

Fig. S16 High resolution Mn 2p and O 1s XPS spectra for pure and acid/alkaline-treated MnO$_2$.

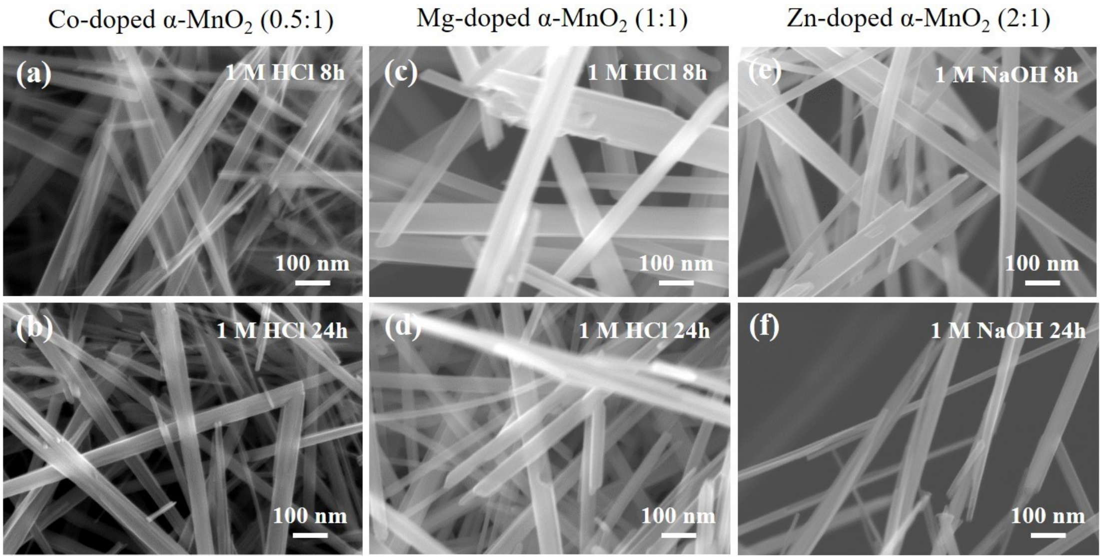

Fig. S17 SEM images of (a, b) Co-doped α-MnO$_2$ (0.5:1), (c, d) Mg-doped α-MnO$_2$ (1:1), and (e, f) Zn-doped α-MnO$_2$ (2:1) with different acid/alkaline treatment conditions.

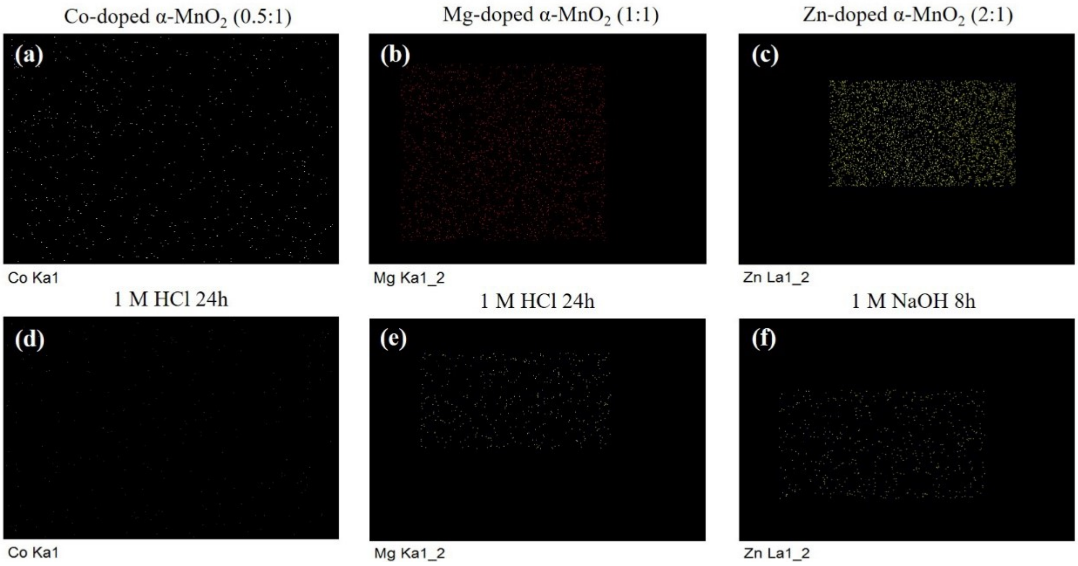

Fig. S18 EDS mapping results of Co-doped α-MnO_2 (0.5:1), Mg-doped α-MnO_2, and Zn-doped α-MnO_2 (2:1) (a-c) before, and (d-f) after acid/alkaline treatment.

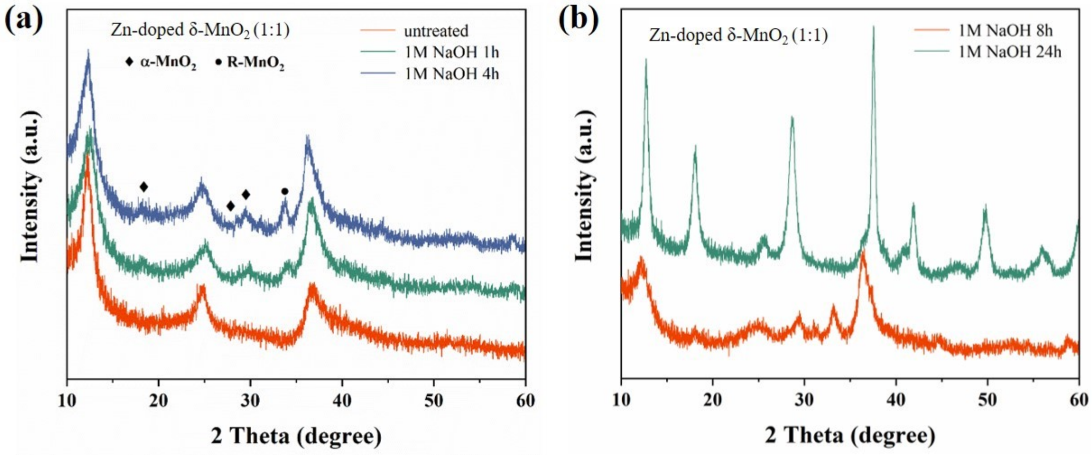

Fig. S19 XRD patterns of Zn-doped δ-MnO_2 (1:1) with different alkaline treatment conditions.

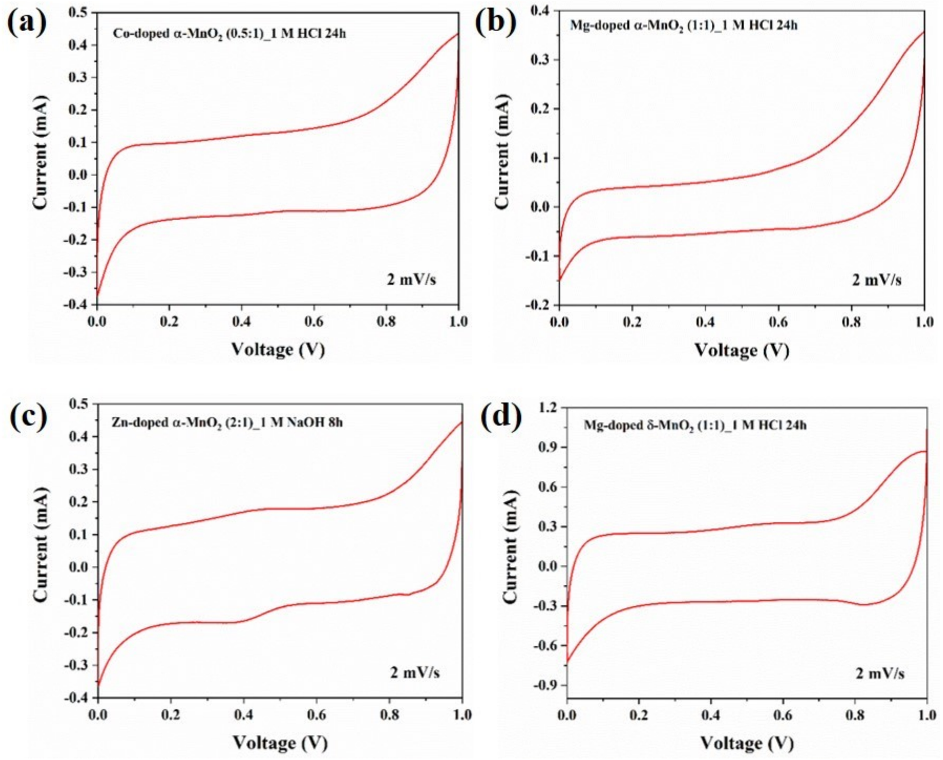

Fig. S20 CV curves measured at 2 mV/s scan rate and in 0-1 V voltage range for as-prepared α/δ-MnO_2 nanostructures with different acid/alkaline treatment conditions.

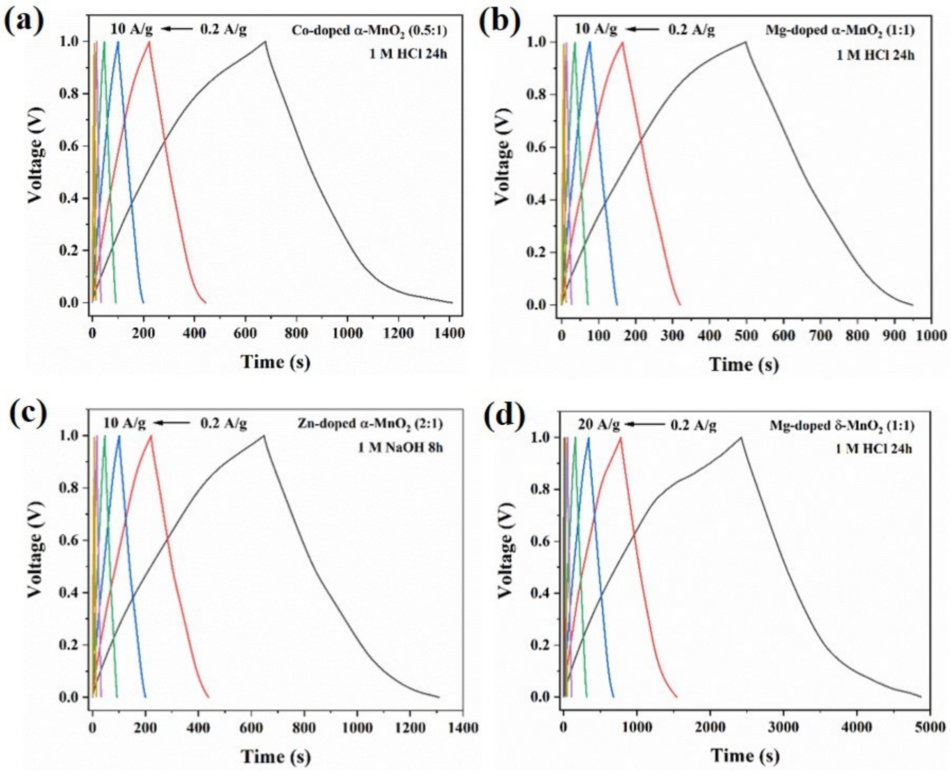

Fig. S21 GCD curves obtained at 0.2-20 A/g current densities and in 0-1 V voltage range for as-prepared α/δ-MnO_2 nanostructures with different acid/alkaline treatment conditions.

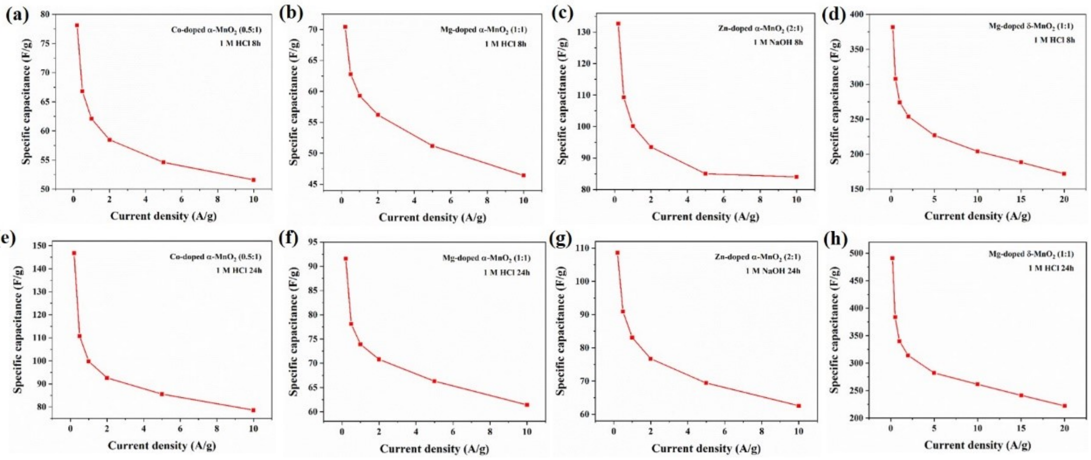

Fig. S22 Specific capacitances vs. current densities for as-prepared α/δ-MnO_2 nanostructures with different acid/alkaline treatment conditions.

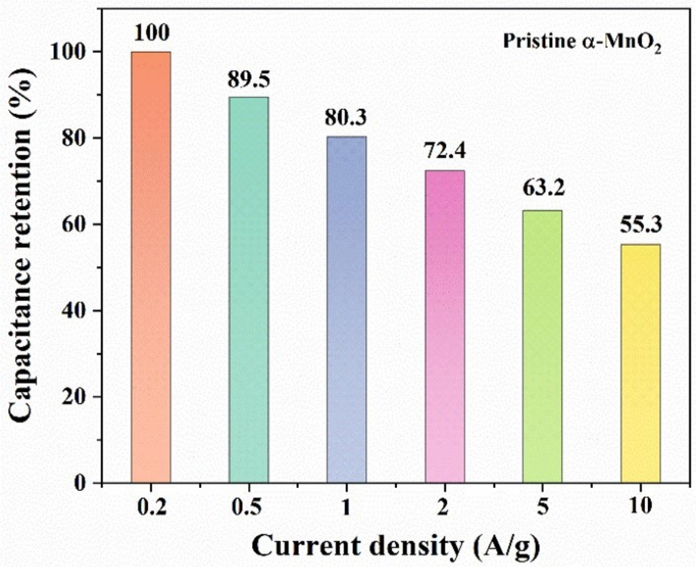

Fig. S23 Capacitance retention vs. current densities for pristine α-MnO_2.

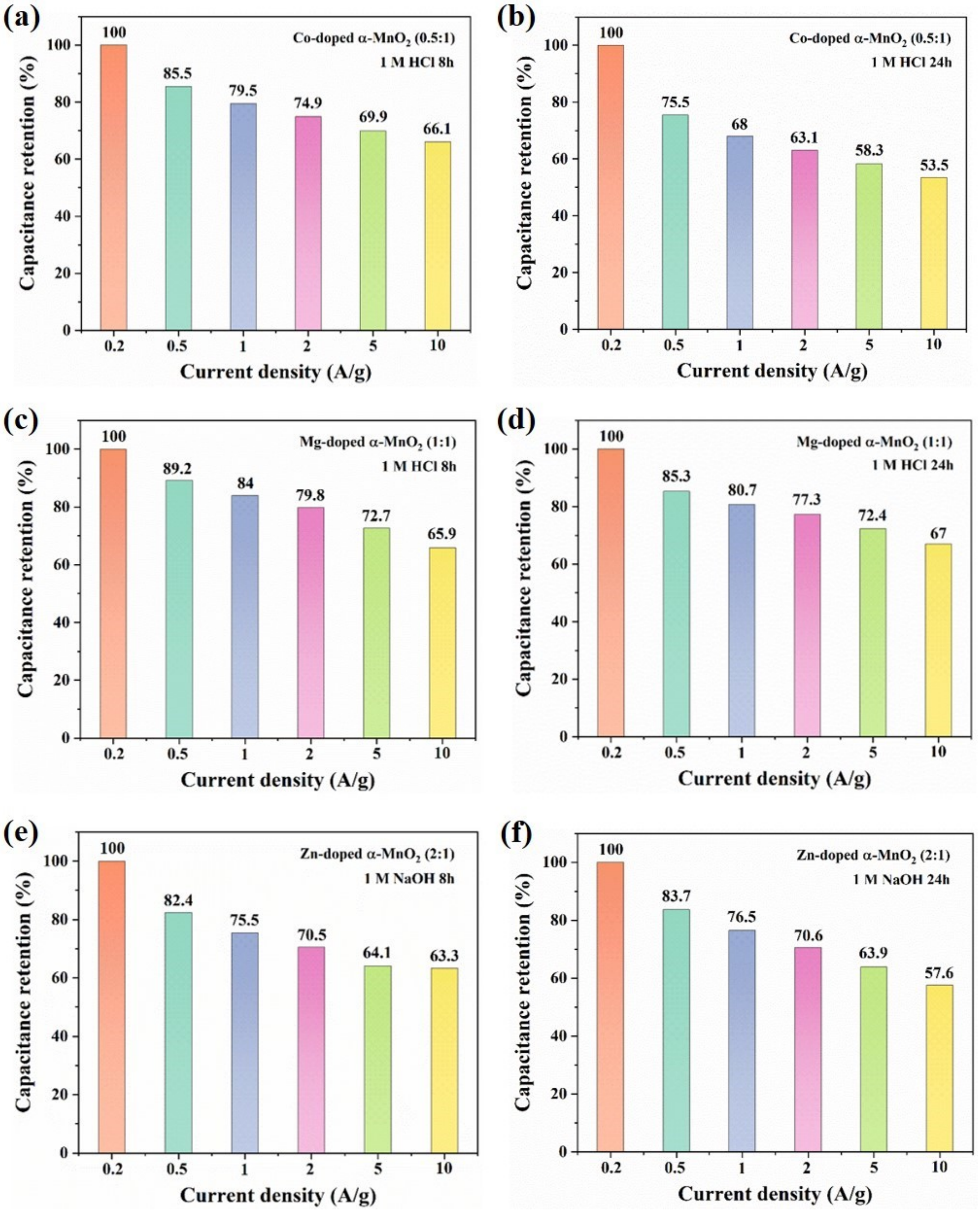

Fig. S24 Capacitance retention vs. current densities for as-prepared α-MnO_2 nanostructures with different acid/alkaline treatment conditions.

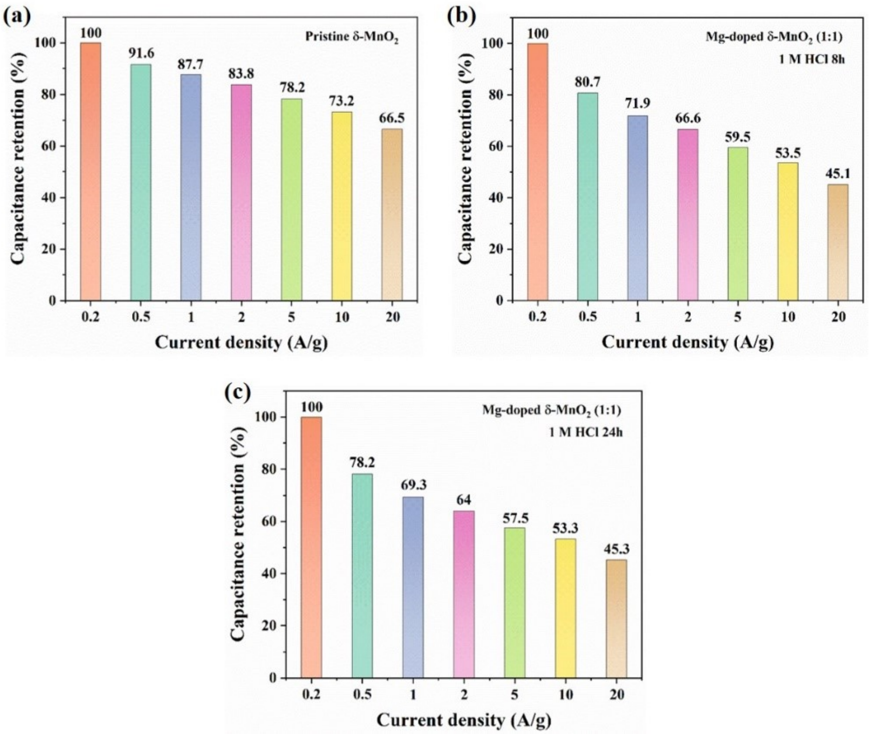

Fig. S25 Capacitance retention vs. current densities for (a) pristine δ-MnO$_2$, and (b, c) δ-MnO$_2$ nanostructures with different acid treatment conditions.

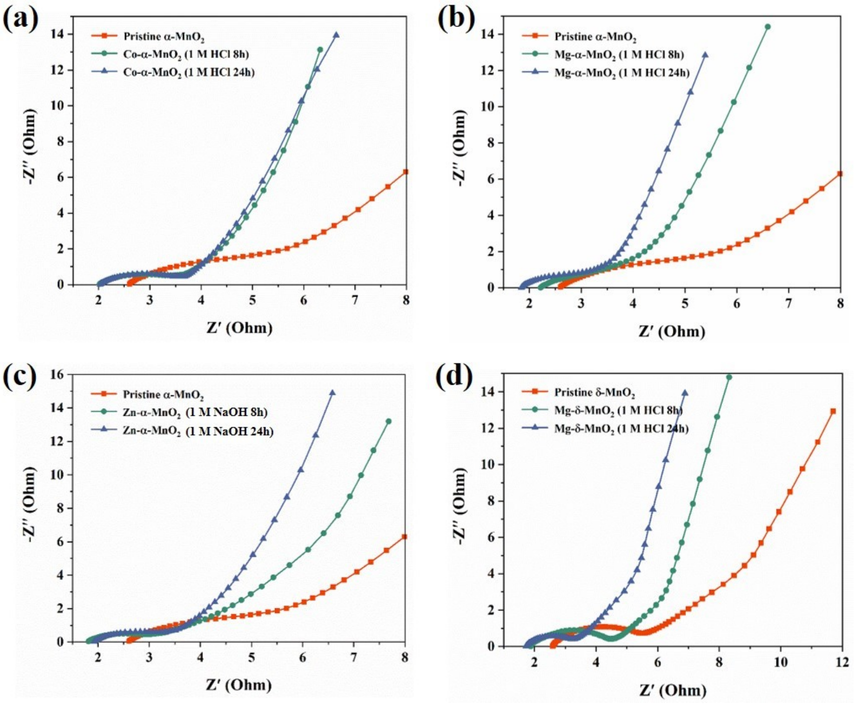

Fig. S26 Nyquist plots for pristine and α/δ-MnO$_2$ nanostructures with different acid/alkaline treatment conditions.

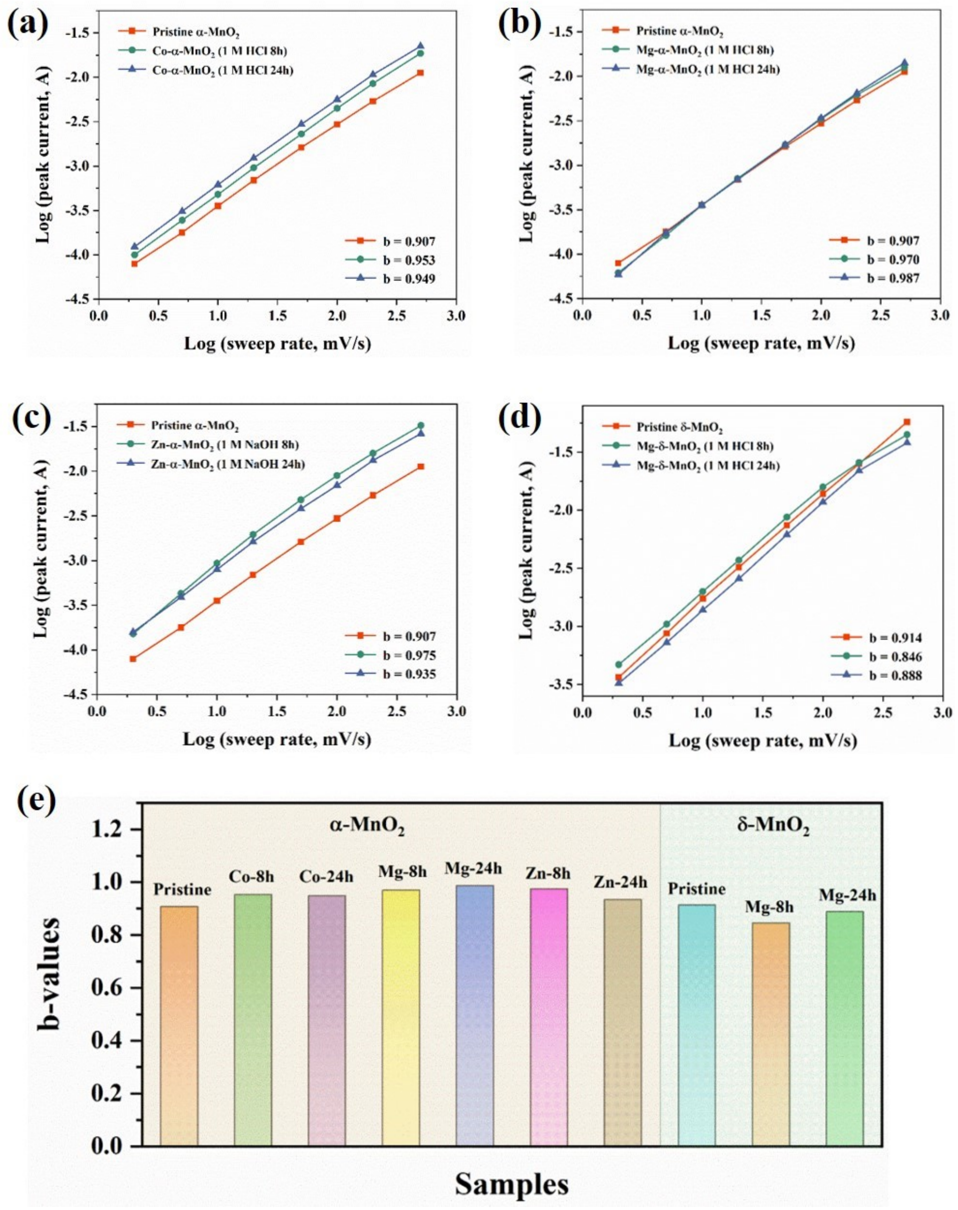

Fig. S27 (a-d) Log (i) vs. log (υ), and (e) b-values comparisons for pristine and α/δ-MnO$_2$ nanostructures with different acid/alkaline treatment conditions.

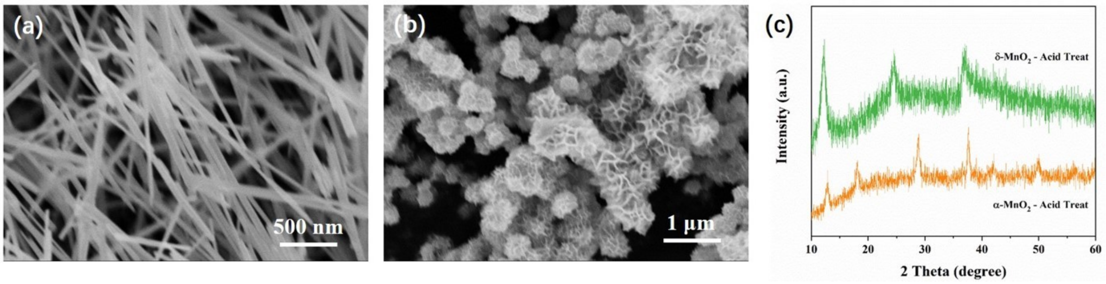

Fig. S28 SEM images of pure (a) α-MnO$_2$, and (b) δ-MnO$_2$ after equilibration in 1 M HCl solution for 24 h. (d) their corresponding XRD patterns.

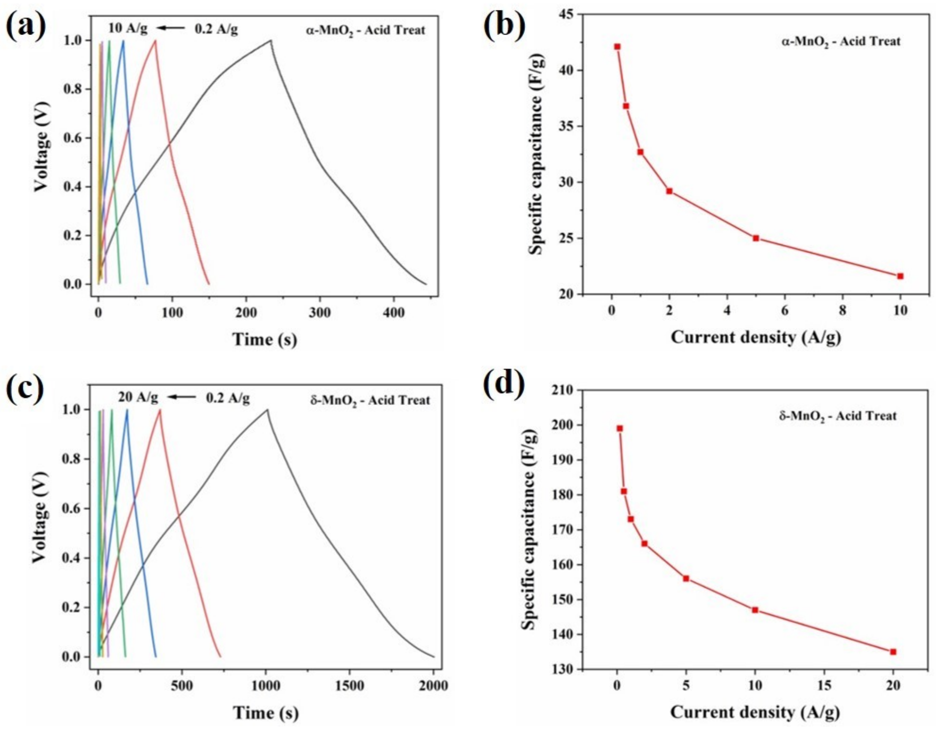

Fig. S29 GCD curves and specific capacitances vs. current densities for acid-treated α/δ-MnO$_2$.

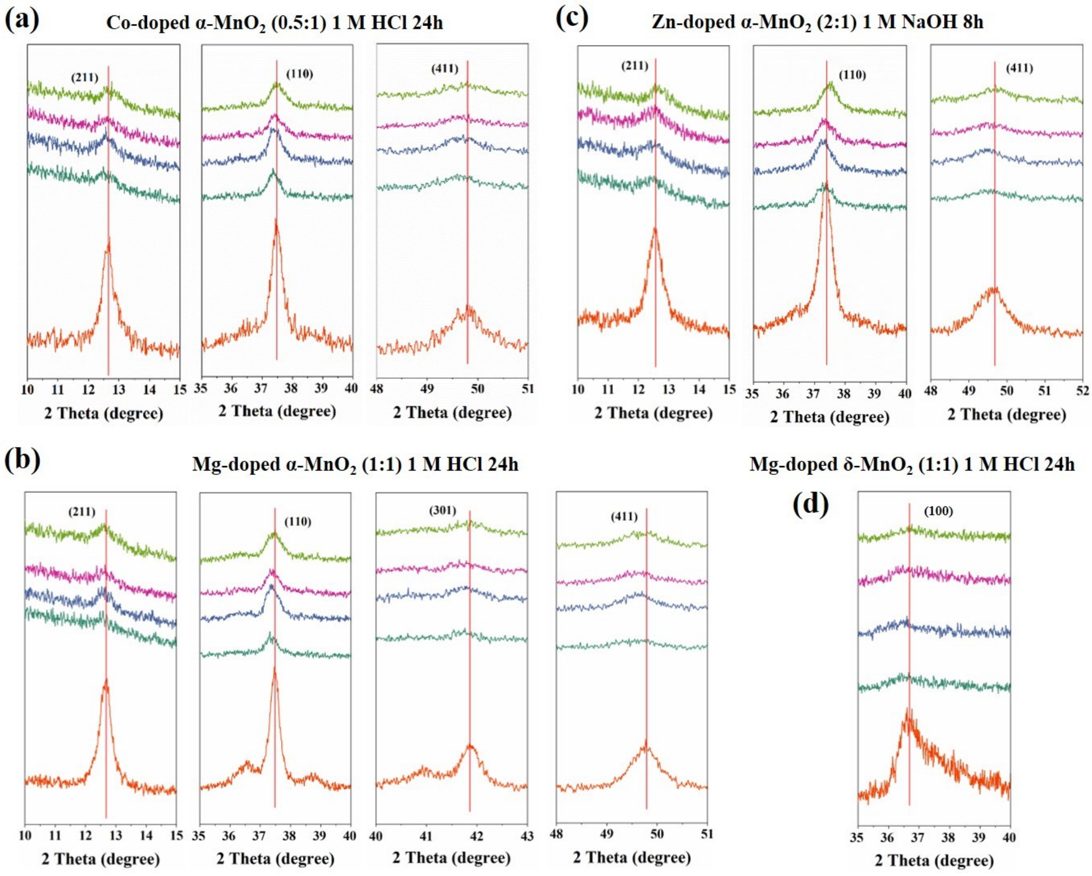

(a) Co-doped α-MnO_2 (0.5:1) 1 M HCl 24h

(c) Zn-doped α-MnO_2 (2:1) 1 M NaOH 8h

(b) Mg-doped α-MnO_2 (1:1) 1 M HCl 24h

(d) Mg-doped δ-MnO_2 (1:1) 1 M HCl 24h

Fig. S30 Ex-situ XRD patterns of as-prepared α/δ-MnO_2 nanostructures with different acid/alkaline treatment conditions.

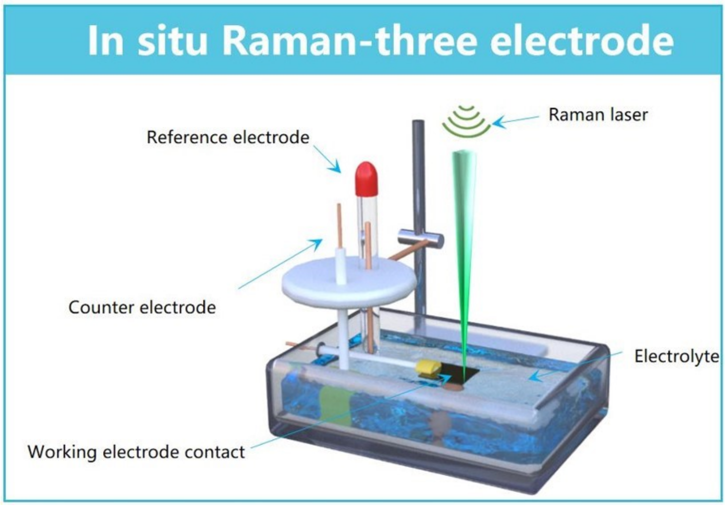

Fig. S31 Schematic diagram showing the in-situ Raman measurement with three electrode setup.

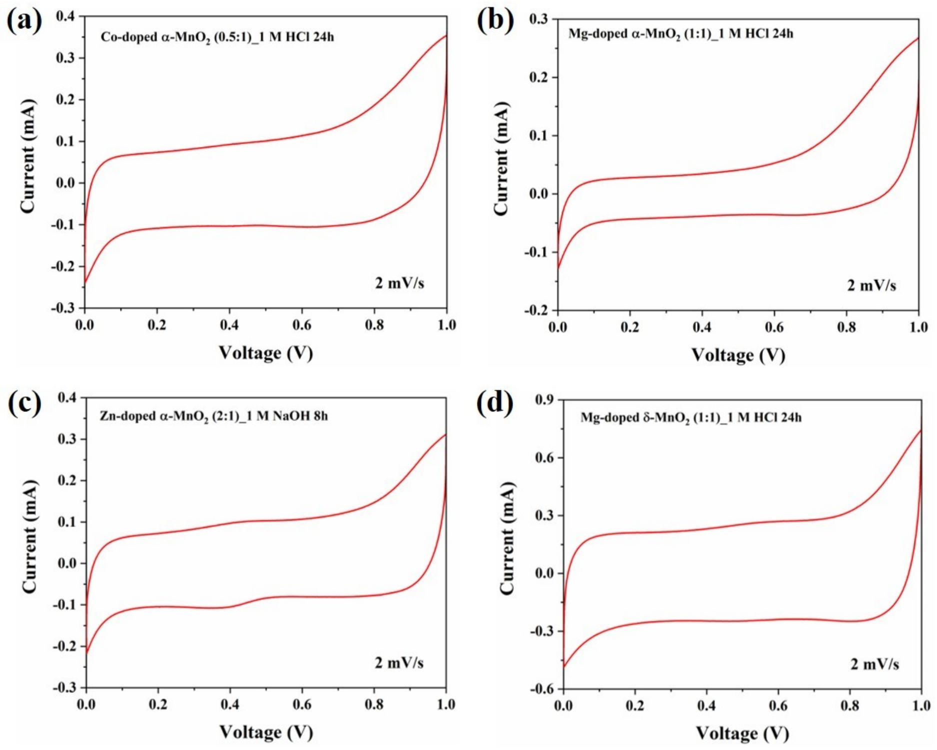

Fig. S32 CV curves of as-prepared α/δ-MnO$_2$ nanostructures with different acid/alkaline treatment conditions using custom-designed in-situ Raman setup.

Table S4 Comparison of supercapacitor performance of various active materials and different modification methods

Electrode materials	Electrolytes	Potential window	Specific capacitances	References
δ-MnO$_2$ with oxygen vacancies	1M Na_2SO_4	0-1 V	286.9 F/g at 1 A/g	[1]
Few layer defective δ-MnO$_2$	1M Na_2SO_4	0-1 V	301.2 F/g at 1 A/g	[2]
Amorphous MnO$_2$ with high Na doping and structural water	1M Na_2SO_4	-0.2-0.8 V	324.7 F/g at 0.5 A/g	[3]
MnO$_2$-carbon composite	6M KOH	-0.6-0.4 V	116 F/g at 2 mA/cm^2	[4]
CF-rGO/CNTs/MnO$_2$	1M Na_2SO_4	-0.2-0.8 V	332.5 F/g at 0.5 A/g	[5]

α-MnO$_2$ nanotube/δ-MnO$_2$ nanoflake/3D graphene foam	1M Na$_2$SO$_4$	0-0.8 V	336 F/g at 2 mV/s	[6]
δ-MnO$_2$/Mn$_2$O$_3$ flower	1M Na$_2$SO$_4$	0-1 V	156.5 F/g at 0.5 A/g	[7]
Zn-doped δ-MnO$_2$	1M Na$_2$SO$_4$	0-1 V	392 F/g at 1 A/g	[8]
C/MnO$_2$/C	6M KOH	-0.2-0.8 V	220 F/g at 1 mA/cm^2	[9]
Free-standing MnO$_2$/CNT	0.5M Na$_2$SO$_4$	0-0.8 V	253.86 F/g at 0.5 A/g	[10]
Ni-doped α-MnO$_2$	2M KOH	0-0.6 V	389.6 F/g at 1 A/g	[11]
Cation vacancies incorporated δ-MnO$_2$	1M Na$_2$SO$_4$	0-1 V	491 F/g at 0.2 A/g, 383.8 F/g at 0.5 A/g	This work

References

[1] A. Q. Zhang, R. Gao, L. Y. Hu, X. G. Zang, R. Yang, S. Y. Wang, S. Y. Yao, Z. Y. Yang, H. G. Hao and Y. M. Yan, *Chem. Eng. J.*, 2021, **417**, 129186.

[2] C. Tang, X. Wang, M. Z. Ma, Z. L. Wang, Y. Li, H. Li, B. Li, Y. X. Zhang and X. B. Zhu, *Chem. Eng. J.*, 2023, **471**, 144784.

[3] H. Bai, S. C. Liang, T. Wei, Q. H. Zhou, M. J. Shi, Z. M. Jiang, J. Feng, M. Y. Zhang, and H. J. Fan, *J. Power Sources*, 2022, **523**, 231032.

[4] L. Chen, F. Wang, Z. W. Tian, H. T. Guo, C. Y. Cai, Q. J. Wu, H. J. Du, K. M. Liu, Z. F. Hao, S. J. He, G. G. Duan, and S. H. Jiang, *Small*, 2022, **18**, 2201307.

[5] C. Tang, K. Zhao, Y. F. Tang, F. P. Li, and Q. N. Meng, *Electrochim. Acta*, 2021, **375**, 137960.

[6] M. He, L. L. Cao, W. L. Li, X. W. Chang, and Z. Y. Ren, *J. Alloys. Compd.*, 2021, **865**, 158934.

[7] F. Qiao, W. J. Liu, S. H. Yu, Q. L. Zhang, G. D. Li, and H. Q. Chu, *Ceram. Int.*, 2024, **50**, 351-359.

[8] J. H. Wu, W. Raza, P. Wang, A. Hussain, Y. B. Ding, J. Yu, Y. Y. Wu, and J. Zhao, *Electrochim. Acta*, 2022, **418**, 140339.

[9] E. S. Kim, H. J. Lee, and B. H. Kim, *Electrochim. Acta*, 2022, **406**, 139883.

[10] Z. H. Li, D. W. Xiao, C. Y. Xu, Z. W. Li, S. Bi, H. Xu, H. Dou, and X. G. Zhang, *J. Mater. Sci.*, 2022, **57**, 8818-8827.

[11] J. W. Zhang, L. B. Zhu, H. T. Jia, K. X. Wei, and L. X. Wen, *J. Alloys. Compd.*, 2021, **889**, 161772.